

Article

# High-Bandwidth Morphing Actuator for Aeroelastic Model Control

Sebastiano Fichera <sup>1,\*</sup>, Irma Isnardi <sup>1</sup> and John E. Mottershead <sup>1</sup>

<sup>1</sup> University of Liverpool, School of Engineering, Liverpool L69 3GH, United Kingdom

\* Correspondence: s.fichera@liverpool.ac.uk; Tel.: +44 (0)151 794 4816

Version January 28, 2019 submitted to Aerospace

**Abstract:** The design and testing of a high-bandwidth continuous actuator for aeronautical applications is presented hereinafter. The actuator has a dual goal of controlling both the aeroelastic behaviour and the flight mechanics of the model in which it is installed. In order to achieve these aims, the actuation bandwidth of the active aerofoil, as well as its static camber variation, have to be sufficiently high. The camber morph is achieved by using tailored piezoelectric patches in a sandwich configuration with a linear trailing edge slider to allow the necessary compliance. The morphing actuator is designed for a NACA 0018 aerofoil with a chord of 300 mm and a span of 40 mm. Static and dynamic experimental tests are carried out on a prototype, and a camber variation control technique is implemented. It is proved that the actuator bandwidth is up to 25 Hz and the equivalent maximum deflection is  $\pm 15$  degrees. This solution is shown to be a viable light-weight alternative to the conventional brushless/servo-motor approach currently used in aeroelastic models.

**Keywords:** high bandwidth; morphing; piezoelectric actuator; aeroelastic wind tunnel model

## 1. Introduction

One of the main challenges during the development of aeroelastic models is the design of the control-surface actuation system. Certain requirements, such as the maximum flap deflection and hinge moment, are dictated by the flight mechanics (i.e. the operational dynamic pressure), while the required actuation bandwidth depends upon the dynamic behaviour of the entire structure and the control objective. To introduce active vibration/flutter suppression techniques, it is necessary that the actuation frequency is at least double the natural frequency of the phenomenon to be controlled. The conventional approach uses geared brushless motors, e.g. [1,2], but their size and weight often make it difficult to fit them inside the aeroelastic structure without compromising the original design. Over the past decade, various discrete-flap solutions, featuring piezoelectric elements, have been proposed to overcome such limitations. Ardelean et al. [3] developed a piezo-stack actuator in a V-shaped configuration that is able to produce a control-surface displacement of  $\pm 7$  degrees with a bandwidth of 15 Hz [4], but the system requires a quite significant internal volume and its weight is comparable if not higher than the equivalent traditional electric actuator; moreover, the amount of flap deflection is small and it is subject to freeplay due to the numerous linkages present. Heinze et al. [5] also designed a piezo-stack solution for the actuator of their High Aspect Ratio Wing (HARW) that produces a deflection less than  $\pm 3$  degrees with a bandwidth up to 20 Hz. The tiny deflection makes this configuration unsuitable for a wide range of applications. Both solutions present acceptable bandwidth but are discrete and limited in the maximum displacement. During the early 1990s, advancements in piezoelectric materials allowed to shape them in patches to be embedded in the structures. Preliminary studies on the ability of such materials to alter the camber of an aerofoil were carried out by Lazarus et al. [6], whom explored the feasibility of using strain-actuated adaptive structures to deform a typical wing box section. Barrett et al. [7–9] designed and tested an all-movable control surface actuated

36 through precompressed piezoceramic sheets showing that deflections up to around  $\pm 22$  degrees  
37 with a bandwidth of 11 Hz can be achieved. Pinkerton et al. [10] at the Langley Research Center  
38 developed a piezoelectric actuator based on a THin-layer composite-UNimorph ferroelectric Driver and  
39 sensor, known as "THUNDER", which was able to increase the leading edge camber of a small aerofoil  
40 thereby introducing significant aerodynamic loads change. More recently, the growing interest in the  
41 camber-morphing aerofoil, together with the development of the NASA Langley Research Centre  
42 Macro-Fiber Composite (MFC) Actuator [11,12] - thin, light and flexible unidirectional piezoceramic  
43 fibres formed in rectangular shapes - resulted in a new family of morphing actuators with continuous  
44 flaps and skin-embedded piezopatches. Cobb et al. [13] used six MFC patches to actively-control the  
45 buffet-induced vibrations on the Block 15 F-16 ventral fin. Bilgen et al. [14] developed a bidirectional  
46 variable-camber aerofoil employing eight MFC 8557-P1-type actuators in a bimorph configuration to  
47 construct the active surfaces and a single four-bar (box) mechanism for skin compliance. The fabricated  
48 aerofoil had a 15 mm thickness, a 127 mm chord, and a 133 mm span. Pankonien et al. [15] further  
49 developed this design introducing Synergistic Smart Morphing Ailerons (SSMA) where the compliant  
50 box aerofoil was replaced by a flexural box aileron. Molinari et al. [16] designed and tested a NACA  
51 0012 lightweight ( $< 0.5$  kg) wing (150 mm  $\times$  150 mm  $\times$  80 mm) with a compliant inner structure  
52 where the roll-attitude was controlled by morphing the camber via three MFC M-8557-P1 patches  
53 applied to the Carbon-Fibre-Reinforced Plastic skin of the model. The solution proposed by Debiassi  
54 et al. [17] instead features four MFC M-8557-P1 patches in a sandwich configuration with 0.125 mm  
55 thickness titanium sheet in between. The section studied is a NACA 0015 (150 mm chord and 158 mm  
56 span) with a leading edge linear slider for skin compliance. Both of these solutions were designed  
57 with primarily static objectives and aerofoils were tested at different angles of attack to study the  
58 aerodynamic performance. Their aim was not to provide an alternative to a discrete control surface  
59 but to morph the entire camber of the aerofoil. Even more recently, the same technology was used to  
60 optimise the aerodynamics by changing the wing geometry for the different flight phases [18].

61 However, to the best of the authors knowledge, none of the continuous morphing solutions  
62 presented above are designed specifically for aeroelastic control and they all present limits in terms of  
63 bandwidth, maximum equivalent deflection or size/weight. The goal of this work is to demonstrate  
64 the ability of the proposed design to satisfy the requirements highlighted earlier and, by doing so, to  
65 provide an alternative to the traditional and well-know brushless motor by allowing a simplification  
66 in the model design and a weight reduction, while retaining the necessary high bandwidth, torque  
67 and deflection properties. The proposed actuator is suitable for a wide range of low-speed models (e.g.  
68 Tang et al. [19]), since it satisfies most of the typical wind tunnel aeroelastic actuators requirements  
69 (i.e. actuation bandwidth, hinge moment and maximum deflection - if used for controlling the flight  
70 mechanics as well). The actuator is ultimately intended to be tested as part of a flexible aeroelastic  
71 wing known as MODFLEX (the MODular aeroelastic FLEXible wing) developed at the University  
72 of Liverpool. According to preliminary data obtained by Fichera et al. [20], the requirements of the  
73 High-Bandwidth Morphing Actuator (HBMA) are a bandwidth of up to 20 Hz with an equivalent  
74 static deflection of  $\pm 15$  deg and a hinge moment greater than 0.05 N/m.

75 The contents of this paper are arranged as follows. The design of the high-bandwidth morphing  
76 actuator is presented in Section 2, including details of the MFC configuration chosen and the 3D printed  
77 components. Experimental test results are discussed in Section 3, including static-deflection, static-load  
78 and dynamic tests in sub-Sections 3.1-3.3. The implementation of a low-level PID controller for  
79 displacement control of the morphing sector is given together with experimental results in sub-Section  
80 3.4.

## 81 2. High-Bandwidth Morphing Actuator (HMBA) design

82 The goal of this work is to design, manufacture and test a camber-morphing trailing edge to be  
83 used as an actuator for aeroelastic models in general and specifically for the MODFLEX rig [20]. The  
84 design concept is explained in the present section.

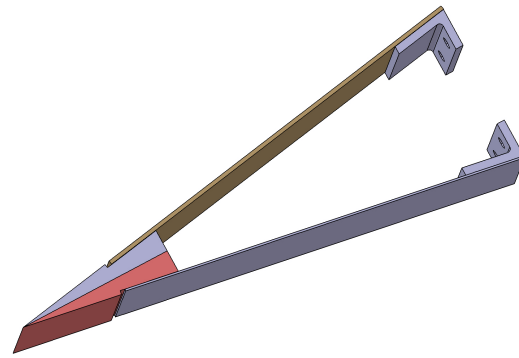
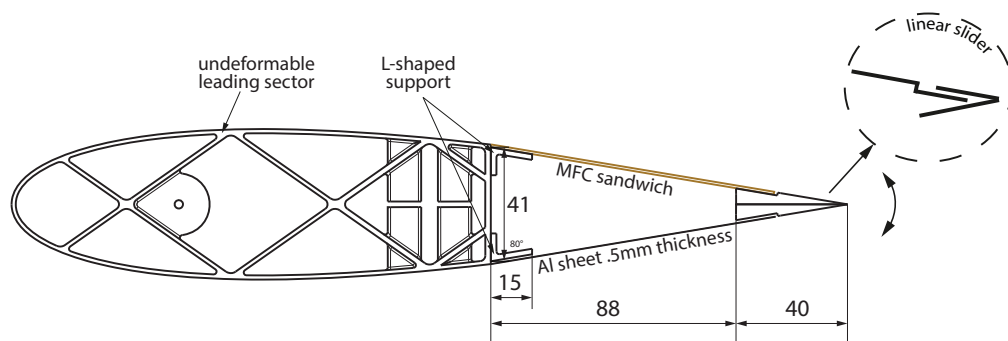
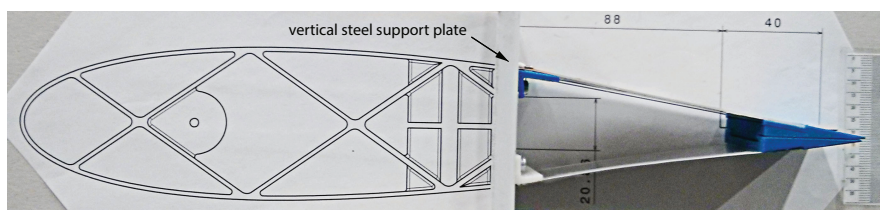


**Figure 1.** High-Bandwidth Morphing Actuator (HMBA).

85 The HBMA, shown in Figure 1, is composed of two sheets, one of which is an MFC piezo-patch  
 86 sandwich and the other a 0.5 mm thickness aluminium sheet. Both sheets are fixed at one end to  
 87 the undeformable main aerofoil structure by L-shaped ABS<sup>1</sup> plastic brackets, and male and female  
 88 T-shaped sliders are attached at the other ends of the MFC sandwich and aluminium sheet, respectively,  
 89 to provide the necessary compliance. The overall dimensions of the actuator are 128 mm length (of  
 90 which 88 mm unsupported) and 40 mm width, and the total mass is 30 g. Figure 2 shows the side  
 91 view of the actuator, including the engineering drawing with principal dimensions (Figure 2a) and a  
 photograph of the tail section (Figure 2b). Figure 3 shows the design of the linear T slider. The length



**(a) Drawing.**



**(b) Experimental.**

**Figure 2.** Side view of the actuator (dimensions in mm).

92 of the T portion was chosen in order to allow  $\pm 7.5$  mm of linear sliding which ensures up to  $\pm 20$  deg  
 93 and 20 mm of trailing edge displacement. Detailed dimensions may be obtained from the authors  
 94 upon request.  
 95

<sup>1</sup> ABS: Acrylonitrile butadiene styrene.

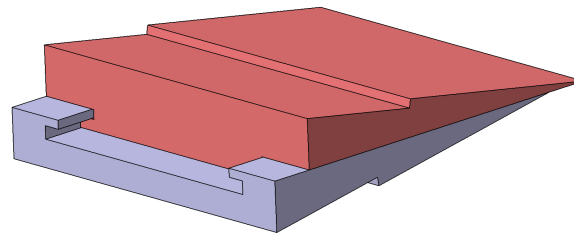


Figure 3. Trailing edge slider.

### 96 2.1. Actuator configuration

97 The NASA Langley Research Centre Macro-Fibre Composites (MFC) are orthotropic actuators  
 98 consisting of unidirectional piezoceramic fibres embedded in an epoxy matrix and sandwiched between  
 99 two polyimide films with an interdigitated electrode pattern that is used for both poling and actuation  
 100 [11]. The major actuation is along the direction of the piezoceramic fibres exploiting the  $d_{33}$  parallel  
 101 effect that corresponds to the deformation of the specimen in the direction of the driving electric field.  
 102 The actuation of MFC actuators, prepackaged as patches, is accomplished by applying an asymmetrical  
 103 voltage between  $-500$  V and  $+1500$  V leading to asymmetrical actuation behaviour, the maximum  
 104 contraction being one third of the maximum elongation. Since the piezo-patches generate an in-plane  
 105 effect, it is necessary bond them to a passive material to produce a bending effect. Symmetric bending  
 106 can be achieved with increased blocking force, but at the cost of reduced bending deformation, by  
 107 bonding together two piezo-patches in an antagonistic configuration.

108 The thickness and mechanical properties of the passive material in the piezo-patch sandwich  
 109 were determined by using the bi-metallic strip analogy with the objective of maximizing the bending  
 110 deflection. A stainless steel shim with Young modulus of 210 GPa and 0.012 mm thickness proved to  
 111 be the best solution. A 3-D FE model of this arrangement was then developed in Abaqus following  
 112 the approach proposed by Latalski et al. [21] with the piezo-patches modelled as an orthotropic,  
 113 homogeneous piezoelectric material, and was validated using data released by the manufacturer using  
 114 the analytic results obtained by the bi-metallic strip analogy. Finally, the complete actuator model  
 115 was developed and used to choose the number of piezo-patches and the dimensions and material  
 116 properties of the passive aluminium sheet (0.5 mm thick,  $E=70$  GPa). Figure 4 shows the FE model  
 117 of the HBMA composed of two bodies with the piezo-patches of the sandwich represented by solid  
 118 20-noded, second order elements (Abaqus C3D20E). The stainless steel shim was modelled using  
 119 8-noded shell elements (Abaqus S8R) with piezo-patches bonded on each of them by TIE constrains.  
 120 Electric potential boundary conditions were defined at each end of the piezoelectric sheets ( $-500$  V /  
 121  $+1500$  V and vice versa). The roots of the sandwich and the aluminium sheet were rigidly constrained  
 122 and the tips were fixed by a kinematic constraint to allow sliding.

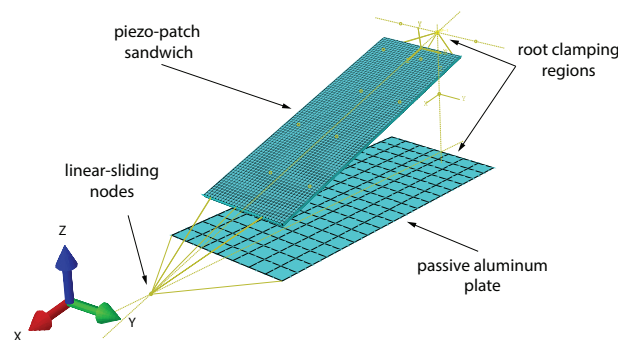
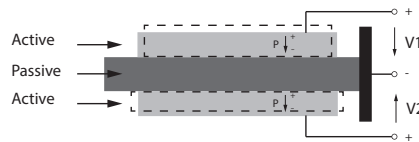


Figure 4. HBMA Abaqus FE model.

123 The sandwich configuration shown in Figure 5 presents two MFCs bonded, one to each side of the  
 124 stainless steel shim with 3M DP460 epoxy glue. Besides increasing the structural stiffness of the skin,



**Figure 5.** Bimorph configurations.

125 this solution allows symmetric deflection of the actuator when operating the two patches around a  
 126 zero deflection condition and doubles the bending blocking force. The drawback of this configuration  
 127 is a decrease in the maximum theoretical deflection from that produced by a single patch plus passive  
 128 material due to the antagonist effect of one patch on the other. Internal ribs, within the actuator inner  
 129 volume, were deemed to be unnecessary because has been demonstrated [14,22] that the out-of-plane  
 130 deformation of the skins due to the aerodynamic load was negligible for actuators with chord and  
 131 span up to 100 mm and airspeed up to 40 m/s.

## 132 2.2. Actuation design comparison

133 As conclusion of the design process, a comparison between the HBMA and a standard actuator  
 134 was carried out. The so-called standard actuator is the one chosen for the discrete flap of the MODFLEX  
 135 [20] and it has to satisfy the same requirements for which the HBMA has been designed. It is composed  
 136 of a brushless motor (Maxon EC16 60W) plus its related encoder and all the parts necessary to assemble  
 137 it into the wing sector. The electric motor is more difficult to embed into the structure than the  
 138 piezo-patch actuator requiring a tailored design of the structure in order to do so. This increase of  
 139 complexity is accompanied by an increase in weight: the overall weight-per-length (WpL) of the  
 140 HBMA is 7.5 g/cm, whereas for an equivalent chord portion, the WpL of the standard actuator is 21.8  
 141 g/cm.

## 142 3. Experimental Tests

143 The experimental setup is illustrated in Figure 6. Three laser displacement sensors are used to  
 144 read the camber variation at three points along the chord of the morphing actuator, the displacement  
 145 signals are either acquired by a dSPACE<sup>®</sup> real-time system or by a Siemens PLM<sup>®</sup> modal analysis  
 146 setup. The voltage supplied to the piezo-patches is either supplied by the Siemens PLM<sup>®</sup> system  
 147 through dSPACE<sup>®</sup> or directly generated by dSPACE<sup>®</sup>. Two Treka<sup>®</sup> PA05039 high-voltage power  
 148 amplifiers raise the dSPACE<sup>®</sup> output voltage (−2.5 V / +7.5 V) to the required Smart Material<sup>®</sup>  
 149 MFC level (−500 V / +1500 V) by introducing a gain of 200. Since the HBMA presents a sandwich  
 150 configuration, it is necessary to operate the two piezo-patches in an antagonistic manner around a  
 151 non-zero voltage level, i.e. +500 V. The maximum deflection is then achieved supplying one MFC with  
 152 +1500 V while the other with −500 V and vice versa for the opposite maximum deflection. In what  
 153 follows, the percentage convention will be used: 0% refers to the zero-actuator deflection (+500 V for  
 154 both the MFCs), 100% refers to the maximum deflection (+1500 V for one MFC and −500 V for the  
 155 other). Following the standard aeronautical convention, the downward deflection of the trailing edge  
 156 is considered positive. To be noticed that the in all the tests presented here the piezo-patch sandwich  
 157 is bonded to the upper skin and the aluminium plate constitutes the lower one.

### 158 3.1. Static Deflection Test

159 A static deflection test was carried out on the morphing rig previously described. The actuator  
 160 was supplied with a control input from 0% to 100% with increments of 25%, following the percentage  
 161 convention presented earlier. This resulted in positive and negative displacements of the trailing edge,  
 162 depending upon the combined polarity of the voltage. The displacements recorded by the three sensors  
 163 are plotted in Figure 7a together with the error bars of their standard deviation; the results obtained  
 164 by the FE model are given by the dashed lines. The deformation proved to be almost linear in both

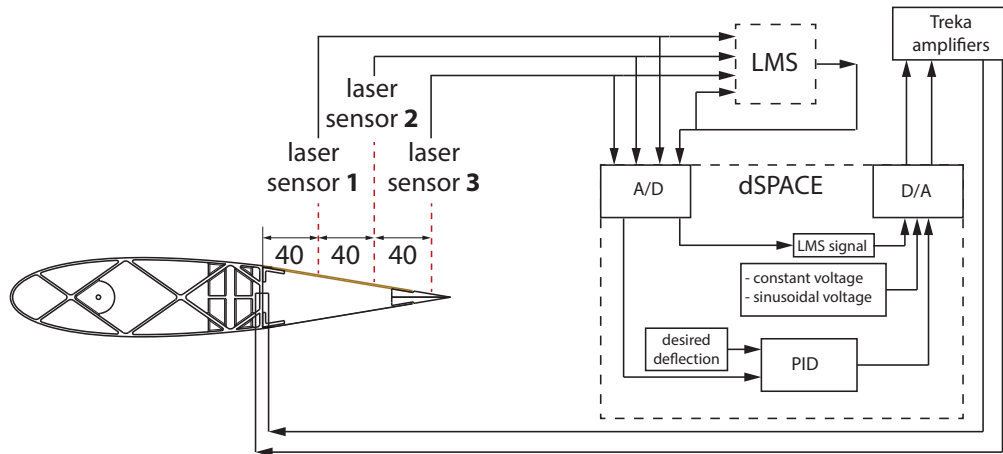
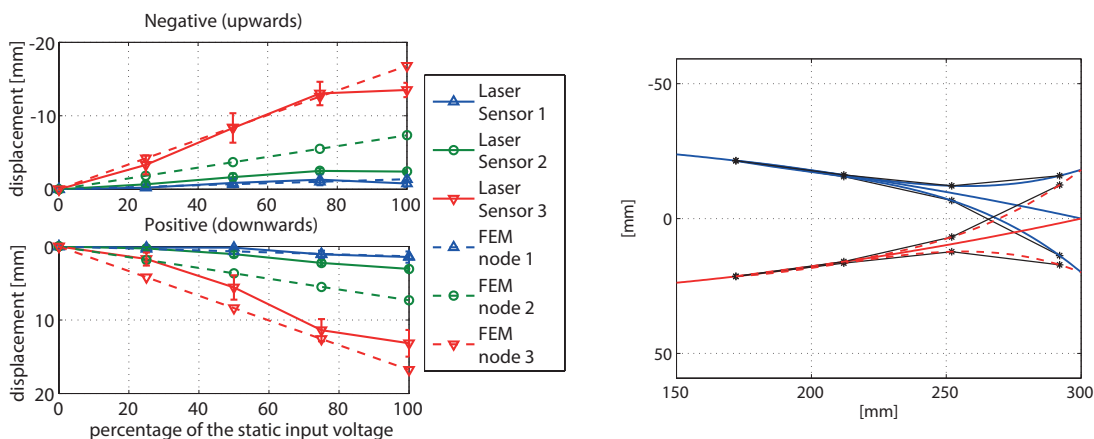


Figure 6. Experimental setup block scheme (dimensions in mm).

165 directions reaching a maximum trailing edge displacements of  $-15$  mm and  $+13$  mm, respectively.  
 166 The normalised RMS error (between the FE and the experimental results) is 0.2 for the first and third  
 167 laser sensor readings but increases to around 2 for the second reading. The discrepancy seems to  
 168 be due to differences in the camber shape along the MFC sandwich. In the experimental model, the  
 169 deflection is concentrated in the portion of the actuator close to the trailing edge, while in the FE model  
 170 it is more evenly distributed along the whole length of the piezo-patches. This different behaviour  
 171 can be explained as a consequence of the presence of the two gluing areas, with the L-shaped support  
 172 and the linear slider, that alter the ability of the piezo-patch sandwich to deform as per design. The  
 173 lower diagram of Figure 7a shows that the positive deflection is slightly smaller than the negative  
 174 one, possibly due to the design choice that features the active element only on the upper skin. The  
 175 reconstructed maximum positive and negative deformations are shown in Figure 7b. The continuous  
 176 lines are the third order polynomial interpolation of the measured displacements while the dashed ones  
 177 represent the lower skin FE displacement prediction. Figure 8 depicts the two maximal deformation of  
 178 the actuator in the positive and negative directions, both numerical and experimental.



(a) Experimental and numerical 3 points displacements.

(b) Reconstructed deformed aerofoil.

Figure 7. HBMA static displacement test.

### 179 3.2. Static Load Test

180 Static load tests were conducted at the maximum negative deflection and a mass hung from the  
 181 trailing edge, as shown in Figure 9a. The load was increased from 0 g to 110 g with intermediate values  
 182 of 10 g and 60 g. Experimental results are shown as continuous lines in Figure 9c, whereas the dashed  
 183 lines represent FE predictions. The lower diagram of Figure 9c shows the deflections under the same

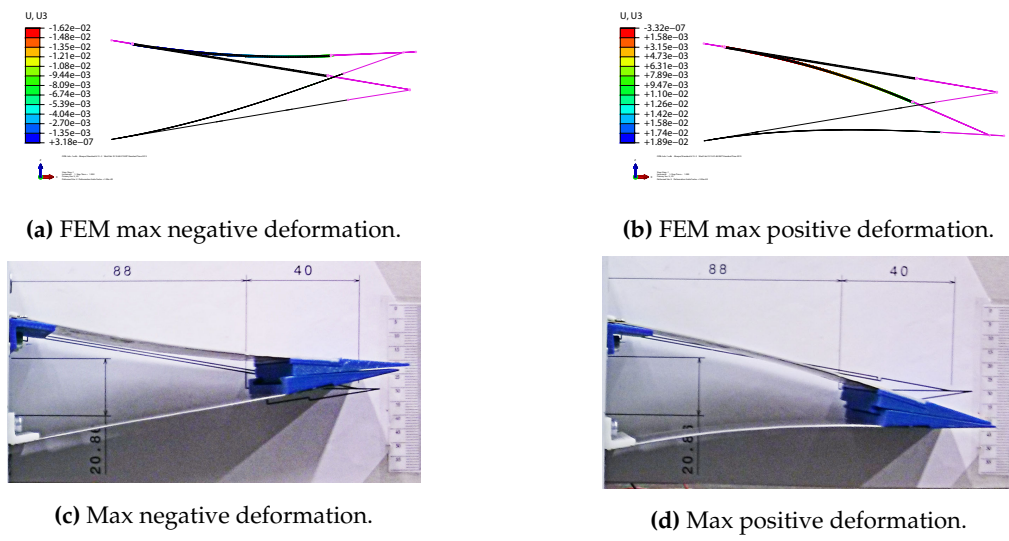


Figure 8. HBMA static deformation.

184 load, but without any voltage applied. The numerical model is seen to be stiffer than the experimental  
 185 one, which might be due to softer L-shaped brackets and other manufacturing imperfections in the  
 186 constraints of the experimental model. The morphing actuator was found to be capable of delivering a  
 187 force at the trailing edge of a 1 N approximately. Considering the length of the actuator, its "equivalent"  
 188 stall torque was determined to be greater than 0.1 Nm, enough to fulfil the hinge moment requirements  
 189 of similar-size aeroelastic models.

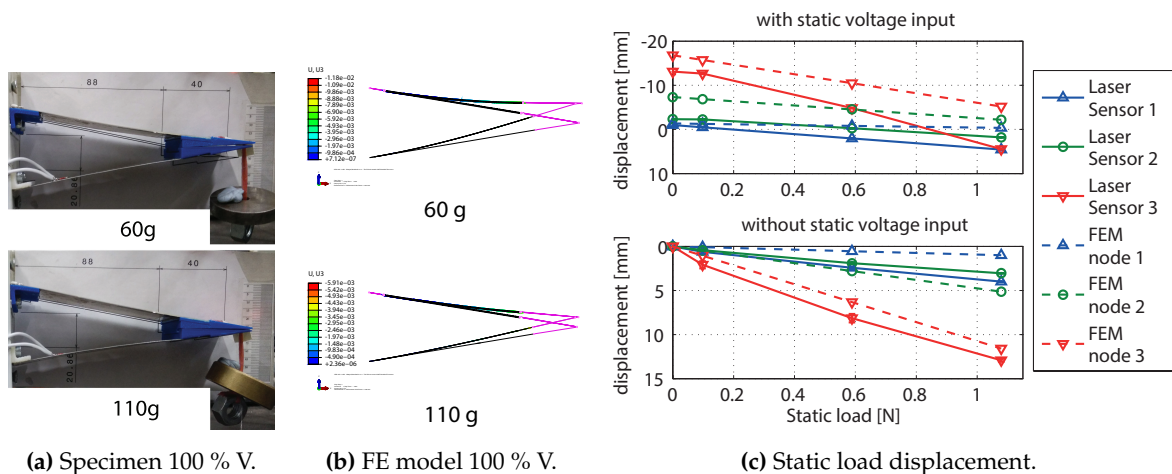
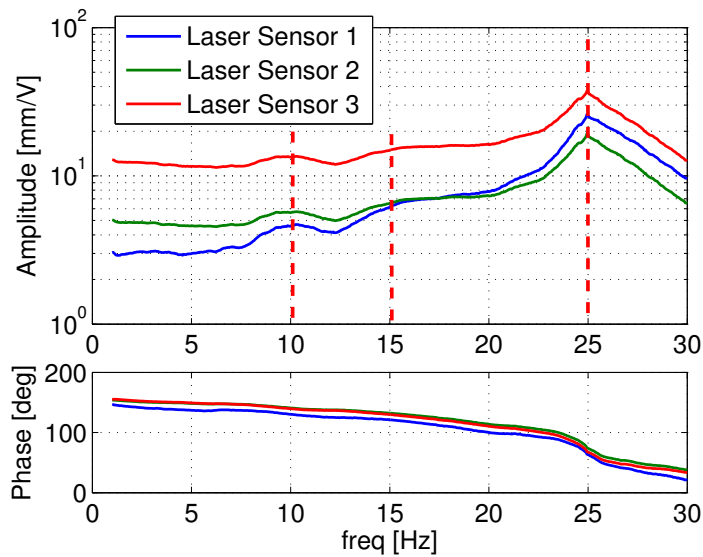


Figure 9. Actuator static load test.

190 **3.3. Dynamic Test**

191 A dynamic test campaign was carried out with the purpose of verifying that the bandwidth of the  
 192 HBMA was greater than 20 Hz and to provide an insight into the dynamic behaviour of the system.  
 193 For this test, the numerical comparison is not provided since the FE model is not capable of predicting  
 194 the dynamic behaviour being not representative of mass and friction of the experimental actuator.  
 195 A stepped-sine modal test was carried out using a Siemens PLM<sup>®</sup> system with a frequency range  
 196 from 1 to 30 Hz, a resolution of 0.05 Hz and delay of 7 cycles. The results are shown in Figure 10 and  
 197 Table 1, which summarises frequencies and damping ratios computed by the PolyMAX algorithm [23].  
 198 Two low-frequency poles appear to be present and were traced to resonances in the wooden support  
 199 structure through which the HBMA was attached to the test table - this conclusion is supported by the



**Figure 10.** Frequency Response Function of the HBMA.

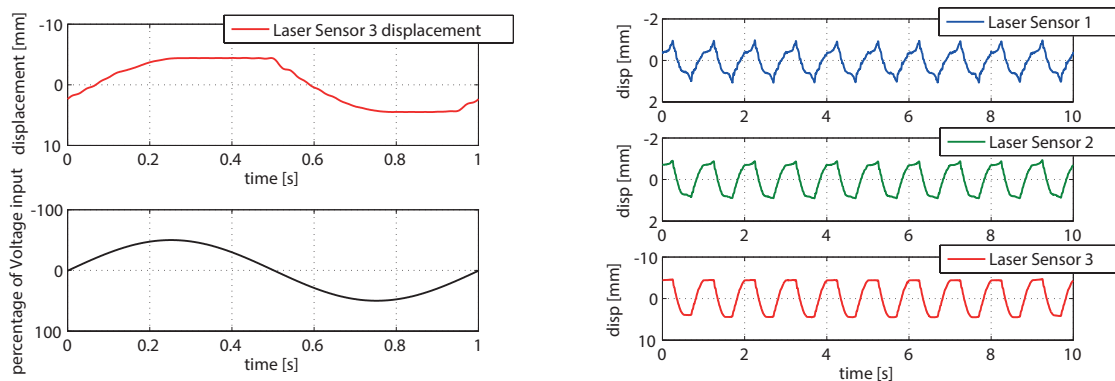
200 apparent high damping levels associated with these modes and to the absence of associated phase-shift.  
 201 The single significant resonance, showing a clear phase shift, occurring at 25 Hz, is the first bending  
 202 mode of the actuator. The observed dynamic behaviour of the HBMA is deemed adequate for the  
 203 intended goals and its transfer function, in the bandwidth of interest, is flat enough to allow the use of  
 204 the actuator in aeroelastic models, once paired with a controller.

	freq [Hz]	$\zeta$ [%]
Actuator support 1 <sup>st</sup> mode	10.97	18.9
Actuator support 2 <sup>nd</sup> mode	15.3	8.8
HBMA first bending mode	24.95	4.4

**Table 1.** Frequencies and Damping.

205 **3.4. Ability of the actuator to follow a prescribed motion**

206 The ability of the HBMA to follow a prescribed motion is investigated as well. The actuator  
 207 is supplied with a sinusoidal input voltage of 50%. The displacements at three locations along the  
 chord of the actuator for a generic 10 s interval is presented in Figure 11. The upper plot in Figure



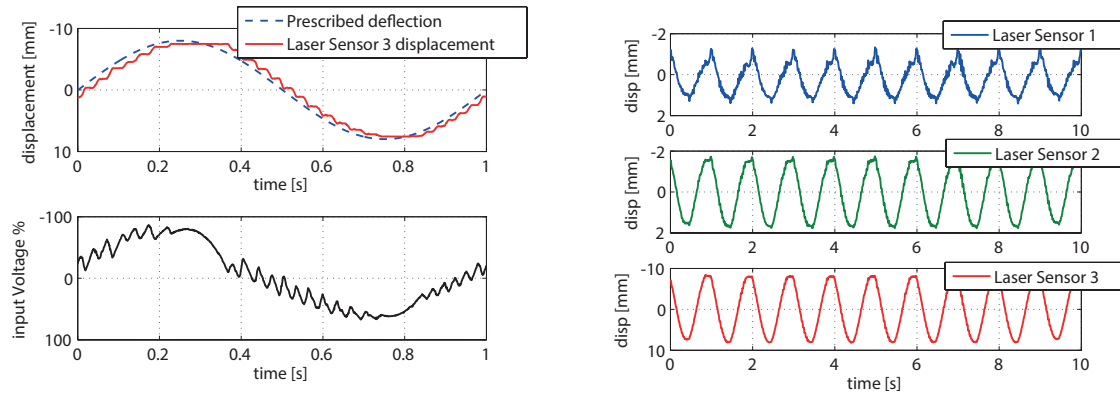
**(a)** Uncontrolled deflection.

**(b)** Uncontrolled 3 laser sensors readings.

**Figure 11.** Uncontrolled: 1 Hz sinusoidal input.



209 11a shows that the uncontrolled actuator reaches an upper and then lower plateau after a ramp  
 210 transition, which is likely to be a consequence of the hysteric behaviour typical of the piezoelectric  
 211 materials. To mitigate this effect, a closed-loop PID controller was implemented. Such a controller  
 212 might form the inner control loop in an aeroservoelastic system, with an outer loop used to implement  
 213 the different control laws for flutter/vibration suppression. Preliminary tuning of the PID controller  
 was achieved by applying the empirical Ziegler-Nichols method [24]. Figure 6 shows the simplified



(a) Deflection controlled by the PID.

(b) Controlled 3 laser sensors readings.

**Figure 12.** Controlled: 1 Hz sinusoidal input.

214 block-diagram scheme for the specimen with the PID controller connected: the reading from the third  
 215 laser displacement sensor is used as position feedback to evaluate the error according to a desired  
 216 deflection through a real-time system. Figure 12 shows the closed-loop actuator displacement response.  
 217 The upper part of Figure 12a shows the prescribed 8 mm displacement of the third laser sensor as  
 218 a dashed line and the physical displacement as the full red line. The percentage voltage supplied  
 219 is shown in the lower figure. The rippling of the control signal is due to amplification of the high  
 220 frequency content of the feedback signal by the derivative term of the PID, which might be alleviated  
 221 by improved tuning of the time constant of the first-order derivative filter as well as introducing a  
 222 low-pass filter applied to the laser sensor feedback signal. It is readily seen, by comparing Figures 12a  
 223 and 11a that the actuator is effective in tracking the desired output. The diagrams of Figures 12b and  
 224 11b show the controlled and uncontrolled displacements measured by the three sensors for a generic  
 225 10 s time history window. The anti-plateau effect of the controller is visible also in the displacement  
 226 signals recorded by the first two laser sensors that indeed show a more sinusoidal behaviour compared  
 227 to the corresponding open-loop responses. The above presented PID controller has been validated in  
 228 the frequency range 1-20 Hz.  
 229

#### 230 4. Conclusions

231 The piezo-patch sandwich paired with a linear trailing edge slider and thin passive aluminium  
 232 sheet has been demonstrated to be a feasible alternative to conventional flap-actuator systems for wind  
 233 tunnel aeroelastic models. Both static and dynamic tests have been carried out on the HBMA, as well  
 234 as the design and test of a preliminary PID inner control loop. The designed actuator fulfils the typical  
 235 aeroelastic models requirements in terms of deflection, bandwidth and torque provided. The actuator  
 236 proved to be able to morph the camber producing a maximum static deflection of its tip equal to 15  
 237 mm and to develop an equivalent torque of 0.1 Nm. Moreover, dynamic tests on the specimen showed  
 238 a bandwidth greater than 20 Hz, suitable for controlling the first elastic modes of most low-speed  
 239 aeroelastic models. From a design viewpoint, the HBMA is lighter than a dynamically equivalent  
 240 brushless motor configuration and may be embedded into the structure straightforwardly without  
 241 affecting the original design. The concept presented in this paper may be scaled in order to achieve  
 242 a greater span of control surface, either by using the wider version of the MFC (e.g. 8557-P1) or by  
 243 arranging rows of the present MFCs. Further improvements in actuator performance might be achieved

244 by using active sandwich components for both the upper and the lower skins and modifying the mass  
 245 of the slider. The T-shaped linear slider was found to be a good trade-off between maximum achievable  
 246 deflection and mechanism robustness, however, alternative sliders designs can be explored to best  
 247 fit different systems requirements and to reduce the trailing edge step effect. The laser displacement  
 248 sensor proved to be adequate in providing the PID feedback signal for the control test rig. However,  
 249 for most experimental aeroelastic studies, independent measurement of the aerofoil section would  
 250 be required in addition. For this reason, a co-located sensing system is now under development. A  
 251 strain gauge, bonded to the passive aluminium sheet, will be calibrated to measure the actuator tip  
 252 deflection.

253 **Author Contributions:** conceptualization, S. Fichera and J.E. Mottershead; investigation, S. Fichera and I. Isnardi.

254 **Funding:** This research was funded by EPSRC, grant number EP/J004987/1, under the project entitled “*Nonlinear*  
 255 *Active Vibration Suppression in Aeroelasticity*”.

256 **Conflicts of Interest:** The authors declare no conflict of interest.

## 257 Abbreviations

258 The following abbreviations are used in this manuscript:

259	HBMA	High Bandwidth Morphing Actuator
	MFC	Macro-Fibre Composites
260	MODFLEX	MODular aeroelastic FLEXible wing
	PID	Proportional Integral Derivative

## 261 References

- 262 1. Ricci, S.; Scotti, A.; De Gaspari, A.; Riccobene, L. Active Aeroelastic Control over a Multisurface  
 263 Wing: Modelling and Wind-Tunnel Testing. *AIAA Journal* **2009**, *47*, 1995–2010. doi: 10.2514/1.34649,  
 264 doi:10.2514/1.34649.
- 265 2. Arena, M.; Amoroso, F.; Pecora, R.; Amendola, G.; Dimino, I.; others. Numerical and experimental  
 266 validation of a full scale servo-actuated morphing aileron model. *Smart Materials and Structures* **2018**.
- 267 3. Ardelean, E.V. High Performance “V-stack” Piezoelectric Actuator. *Journal of Intelligent Material Systems*  
 268 *and Structures* **2004**, *15*, 879–889. doi:10.1177/1045389X04045150.
- 269 4. Papatheou, E.; Wei, X.; Jiffri, S.; Prandina, M.; Tehrani, M.G.; Bode, S.; Singh, K.V.; Mottershead, J.E.;  
 270 Cooper, J. Flutter control using vibration test data: theory, rig design and preliminary results. International  
 271 Seminar on Modal Analysis (ISMA2012); , 2012.
- 272 5. Heinze, S.; Karpel, M. Analysis and Wind Tunnel Testing of a Piezoelectric Tab for Aeroelastic Control  
 273 Applications. *Journal of Aircraft* **2006**, *43*, 1799–1804. doi:10.2514/1.20060.
- 274 6. Lazarus, K.B.; Crawley, E.F.; Bohlmann, J.D.; Worth, F. Static aeroelastic control using strain actuated  
 275 adaptive structures. *Journal of Intelligent Material Systems and Structures* **1991**, *2*, 386–440.
- 276 7. Barrett, R.M. All-moving active aerodynamic surface research. SPIE 2427, Active Materials and Smart  
 277 Structures, 1995, Vol. 2427, pp. 2–15. doi:10.1117/12.200915.
- 278 8. Barrett, R.M.; Gross, R.S.; Brozoski, T.F. Design and Testing of a Subsonic All-Moving Adaptive Flight  
 279 Control Surface. *AIAA Journal* **1997**, *35*, 1217–1219. doi:10.2514/2.217.
- 280 9. Barrett, R.M.; Gross, R.S.; Brozoski, T.F. Missile flight control using active flexspar actuators. *Smart*  
 281 *Materials and Structures* **1999**, *5*, 121–128. doi:10.1088/0964-1726/5/2/002.
- 282 10. Pinkerton, J.L.; Moses, R.W. A Feasibility Study to Control Airfoil Shape Using THUNDER. Technical  
 283 Report 4767, NASA, 1997.
- 284 11. Wilkie, W.; Bryant, R.G.; High, J.W.; Fox, R.L.; Hellbaum, R.F.; Jalink, J.A.; Little, B.D.; Mirick, P.H. Low-cost  
 285 piezocomposite actuator for structural control applications. Proceedings of SPIE, 2000, Vol. 3991, pp.  
 286 323–334. doi:10.1117/12.388175.
- 287 12. Wilkie, W.; G., R.; Fox, R.; Hellbaum, R.F.; High, J.W.; Jalink, J.A.; Little, B.D.; Mirick, P.H.  
 288 Positioning monolithic wafers on backing sheets, joining using adhesives, then slicing into fibers and  
 289 covering with conductive films having electrodes patterns; strain activators, 2003. US Patent 6,629,341.

- 290 13. Browning, J.; Cobb, R.; Canfield, R.; Miller, S. F-16 Ventral Fin Buffet Alleviation Using  
291 Piezoelectric Actuators. 50th AIAA/ASME/ASCE/AHS/ASC Structures, Structural Dynamics, and  
292 Materials Conference; American Institute of Aeronautics and Astronautics: Reston, Virginia, 2009.  
293 doi:10.2514/6.2009-2538.
- 294 14. Bilgen, O.; Kochersberger, K.B.; Inman, D.J.; Ohanian, O.J. Novel, Bidirectional, Variable-Camber Airfoil  
295 via Macro-Fiber Composite Actuators. *Journal of Aircraft* **2010**, *47*, 303–314. doi:10.2514/1.45452.
- 296 15. Pankonien, A.; Faria, C.T.; Inman, D. Synergistic Smart Morphing Aileron. 54th  
297 AIAA/ASME/ASCE/AHS/ASC Structures, Structural Dynamics, and Materials Conference; American  
298 Institute of Aeronautics and Astronautics: Reston, Virginia, 2013. doi:10.2514/6.2013-1512.
- 299 16. Molinari, G.; Quack, M.; Arrieta, A.F.; Morari, M.; Ermanni, P. Design, realization and structural testing of  
300 a compliant adaptable wing. *Smart Materials and Structures* **2015**, *24*, 105027.
- 301 17. Debiasi, M.T.; Chan, W.L.; Jadhav, S. Measurements of a Symmetric Wing Morphed by Macro Fiber  
302 Composite Actuators. 54th AIAA Aerospace Sciences Meeting, 2016, p. 1565.
- 303 18. Li, D.; Zhao, S.; Da Ronch, A.; Xiang, J.; Drofelnik, J.; Li, Y.; Zhang, L.; Wu, Y.; Kintscher, M.; Monner, H.P.;  
304 others. A review of modelling and analysis of morphing wings. *Progress in Aerospace Sciences* **2018**.
- 305 19. Tang, D.; Dowell, E.H. Experimental and Theoretical Study on Aeroelastic Response of High-Aspect-Ratio  
306 Wings. *AIAA Journal* **2001**, *39*, 1430–1441. doi:10.2514/2.1484.
- 307 20. Fichera, S.; Jiffri, S.; Mottershead, J.E. Design and wind tunnel test of a MODular aeroelastic FLEXible  
308 wing (MODFLEX). Proceedings of the International Conference on Noise and Vibration Engineering ISMA  
309 2016; , 2016.
- 310 21. Latalski, J. Modelling of macro fiber composite piezoelectric active elements in ABAQUS system.  
311 *Eksploatacja i Niezawodność - Maintenance and Reliability* **2011**, *1*, 72–78.
- 312 22. Debiasi, M.T.; Bouremel, Y.; Lu, Z.; Ravichandran, V.; Khoo, H.H.; Luo, S. Deformation of the  
313 Upper and Lower Surfaces of an Airfoil by Macro Fiber Composite Actuators. 31st AIAA Applied  
314 Aerodynamics Conference; American Institute of Aeronautics and Astronautics: Reston, Virginia, 2013.  
315 doi:10.2514/6.2013-2405.
- 316 23. Peeters, B.; Auweraer, H.V.D.; Guillaume, P.; Leuridan, J. The PolyMAX frequency-domain method: a new  
317 standard for modal parameter estimation? *Shock and Vibration* **2004**, *11*, 395–409. doi:10.1155/2004/523692.
- 318 24. Aström, K.J.; Hägglund, T. *PID Controllers: Theory, Design, and Tuning*, 2 ed.; Instrument Society of America,  
319 Research Triangle Park, NC, 1995.